

HYDROGEN EMBRITTLEMENT OF ULTRAFINE-GRAINED AUSTENITIC STAINLESS STEELS

E. G. Astafurova, S. V. Astafurov, G. G. Maier, V. A. Moskvina, E. V. Melnikov and A. S. Fortuna

Institute of Strength Physics and Materials Science, Siberian Branch of Russian Academy of Sciences, 2/4 Akademicheskoy avenue, 634055 Tomsk, Russia

Received: June 04, 2018

Abstract. The effect of electrochemical hydrogen-charging on tensile properties, mechanisms of plastic deformation and fracture micromechanisms was studied using two ultrafine-grained (UFG) Cr-Ni austenitic stainless steels. UFG austenitic structures with an average subgrain size of 200 nm for CrNiMo (316L-type) and 520 nm for CrNiTi (321-type) steel were produced using hot-to-warm ABC-pressing. Hydrogen-charging up to 100 hours weakly influences stages of plastic flow, strength properties and elongation of the UFG steels. TEM analysis testifies to hydrogen-assisted partial annihilation and rearrangement of dislocations into dislocation tangles, and to hydrogen-induced variation in ratio of low- and high-angle misorientations in UFG structure of both steels. Hydrogen-alloying promotes mechanical twinning and deformation-induced $\gamma \rightarrow \epsilon$ martensitic transformation in the UFG steels under tension. Ultrafine-grained CrNiTi steel with lower stacking fault energy (SFE) is more susceptible to mechanical twinning and deformation-induced $\gamma \rightarrow \epsilon$ martensitic transformation in comparison with CrNiMo steel with higher SFE. The micromechanism of the fracture in hydrogen-assisted surface layers of the steels is compositional, grain-size and hydrogen content dependent characteristic. The present results demonstrate that the steels with UFG structure possess higher resistance to hydrogen embrittlement compared to coarse-grained analogues.

1. INTRODUCTION

Hydrogen embrittlement (HE) is one of the most notable property of hydrogen in conventional coarse-grained (CG) austenitic steels. HE depends on a wide range of parameters, in particular, on the stacking fault energy (SFE), chemical and phase composition of the steels, hydrogen saturation method, temperature, strain rate, etc. [1-3]. In some studies, authors considered that metastable austenitic steels suffer from HE due to deformation-induced $\gamma \rightarrow \alpha'$ martensitic transformation [4-6]. Zhang et al. [4] clarified that prior α' -martensite (formed by pre-strained) possesses little relation with HE effect, but dynamic $\gamma \rightarrow \alpha'$ martensitic transformation contributes to HE more effectively. Therefore, a stabil-

ity of austenite against deformation-induced $\gamma \rightarrow \alpha'$ martensitic transformation can be considered as positive factor influencing HE in austenitic steels. In addition to aforementioned argument, Michler et al. [7] studied HE in seven austenitic steels of different chemical compositions, which were stable against martensitic transformation. They established that stability of austenite is not a sufficient criterion for the stability of the steel to hydrogen environmental embrittlement, and tensile ductility can be significantly reduced in gaseous hydrogen even in the absence of α' martensite. Other researches [3,5,8] also indicated that austenite can be embrittled by hydrogen in the absence of martensitic phase. Hydrogen-induced effects in steel can be also associated via different mechanisms: hydrogen enhanced

Corresponding author: E.G. Astafurova, e-mail: elena.g.astafurova@gmail.com

localized plasticity (HELP-effect), mechanical twinning, a pseudohydride phase, hydrogen-enhanced decohesion (HEDE-effect), hydrogen assisted cracking (HAC), hydrogen enhanced strain induced vacancy (HESIV) and some others [1-3,9,10].

The susceptibility of austenitic steels to HE is also known to be related to grain size, distribution and density of the lattice imperfections – boundaries, subboundaries, dislocation walls and arrays, chaotically distributed dislocations, etc. The influence of a high density of defects and boundaries of various types can be ambiguous.

The majority of models on hydrogen embrittlement is based on the reaction of hydrogen atoms to dislocations. For this reason, dislocation density plays an important role in HE of steels. Michler et al. [8] suggested that creating of “critical” amount of dislocation increases the susceptibility of CrNiMo (316-type) austenitic steels to HE. They concluded that very high dislocation density in heavily pre-strained steels limits the mean free pass of dislocations, which, in turn, suppresses hydrogen transport and provides high HE of the steels [8]. Han et al. [11] also showed that the mobility of hydrogen atoms in cold-deformed Fe-0.6C-18Mn and Fe-0.6C-18Mn-1.5Al steels decreases in comparison with fully-annealed steels. Mine et al. [12] noticed the increase in hydrogen trapping ability in austenitic stainless steels with ultrafine-grained structures, which possess high dislocation densities.

Mechanical twinning can be assumed as important mechanism, which is attributed with HE in steels possessing low SFE. Han et al. [11] and Astafurova et al. [13] show that increased density of twin boundaries in Fe-Mn-C austenitic steels enhances the effects of steel degradation in hydrogen.

The effect of grain size on the regularities of plastic flow and fracture mechanisms of austenitic steels, subjected to hydrogen saturation, was studied in series of researches [12,14,15]. For metastable austenitic steel Fe-16Cr-10Ni and grain size range of 1–50 μm , Macadre et al. [14,15] shown that HE sensitivity reduced with decrease in grain size. They found a “critical grain size” for HE sensitivity to be about 6 μm – for smaller size hydrogen causes slight decrease in ductility, but for larger ones drastically decreases it. Mine with coauthors [12,16,17] studied the effect of grain boundaries on hydrogen diffusion and hydrogen trapping in CrNi austenitic stainless steels with ultrafine-grained (UFG) structures. They noted an enhanced hydrogen diffusivity and short-circuited diffusion due to increased fraction of grain boundaries in ultrafine-grained structure of the

310 stainless steel [12]. For ultrafine-grained metastable 304 stainless steel, hydrogen-induced ductility loss is partially suppressed compared to solution-treated one [16,17].

The positive effect of reducing of grain size on the HE sensitivity was also shown for precipitation strengthened Fe-Ni alloy, duplex stainless steels, high-strength low-alloy steels in [18-20].

Motivation and the objective of the research

Aforementioned peculiarities of hydrogen-assisted effects in UFG and nanostructured steels show some open questions on this subject. The general problem, concerning the effect of grain refinement on the processes of hydrogen embrittlement in steels, is still not solved. This is due to the wide variety of structural and phase states in steels and large number of external factors influencing steel properties, such as temperature, strain rate, hydrogenation regime, etc. In order to move forward on this issue, it is necessary to set particular experimental tasks on a limited range of materials and to try establishing the influence of each factor.

High-temperature ABC-pressing was used as a deformation method for refinement of grain structure. Similar deformation regime, including multipass hot-to-warm working, were successfully used for refinement of Cr-Ni steels by Belyakov et al. [21]. Multiple high-temperature compressions with change in loading direction by 90° in each pass produce austenitic structure, which contains equiaxed subgrains with high dislocation densities in their interiors and possesses subgrain sizes in submicron range [21]. In this way, we produce ultrafine grain-subgrain single phase austenitic structures with high density of deformation defects, low-angle subboundaries, and high-angle boundaries, which all act as trapping-cites for hydrogen atoms. This allows us to determine the peculiarities of hydrogen absorption, and hydrogen-assisted deformation and fracture mechanisms in steels supersaturated with high density of deformation-assisted defects. High-temperature deformation also eliminates the effect of pre-existed α' -martensite on hydrogen-assisted impact of the ultrafine-grained steels.

Yamabe et al. [22] shown that hydrogen diffusivity and solubility are the same for 300-series steels. Two austenitic 300-series steels with different SFE were chosen for investigation. The first one, metastable Cr-Ni-Ti stainless steel (AISI 321-type), undergoes strain-induced $\gamma \rightarrow \alpha'$ martensitic transformation during straining at room temperature [23].

The second one, Cr-Ni-Mo stainless steel (AISI 316L-type), possesses stable austenitic structure due to rather high SFE [24]. The choice of these two steels gives the opportunity to compare the effect of SFE, i.e., stability of austenitic structure to martensitic transformation and SFE-affected deformation mechanisms, on hydrogen embrittlement of both CG and UFG steels.

Different hydrogen-saturated durations were chosen to evaluate and compare the effect of hydrogen concentration on deformation mechanisms and fracture micromechanisms in CG and UFG steels. This approach is based on different sorption mechanisms in steels with different fraction of grain boundaries, subboundaries and deformation defects.

The objective of the given research is to study the effect of electrochemical hydrogen charging on microstructure and dislocation arrangement, grain/subgrain size, tensile properties and fracture mechanisms in ultrafine-grained austenitic stainless steels processed by hot-to-warm ABC-pressing.

2. MATERIALS AND METHODS

We study two austenitic CrNi stainless steels alloyed with Mo and Ti. The chemical compositions of the steels are shown in Table 1. CrNiTi and CrNiMo steels are Russian analogues of an AISI 321 steel and an AISI 316L-type one.

The initial steel billets were solution-treated at the temperatures of 1050 and 1100 °C for CrNiTi steel and CrNiMo steel respectively. First part of the specimens was thermo-mechanically processed to obtain the UFG structure. Second part of specimens for structural analysis and tensile deformation was cut from the solution-treated billets. These specimens were used as a reference material to show the difference in hydrogen-assisted effects for CG and UFG steels.

For grain refinement, the solution-treated billets were cut into parallelepiped blocks with linear dimensions of 20 × 20 × 40 (mm) and processed by hot-to-warm ABC-pressing. ABC-pressing was performed at the temperature interval 600-800 °C with a decrease in temperature by 50 °C after series of passes (3 to 5) at each temperature. The value of

reduction in each pressing pass was about 55%. For CrNiTi steel, the finish pressing temperature was $T=700$ °C, the further decrease in pressing temperature caused multiple cracking of the billets during upset. For CrNiMo steel, the finish temperature was 600 °C. The details of ABC-pressing process and the microstructure of the steels after plastic deformation were described in [25]. The final cumulative strain after ABC-pressing $\Sigma \varepsilon = \Sigma \ln \varepsilon_i$ (where ε_i – strain for each pressing-pass) are $\Sigma \varepsilon = 6.8$ and $\Sigma \varepsilon = 5.0$ for CrNiMo and CrNiTi steels, respectively.

Electro-discharge machining was utilized to cut regular dumb-bell shaped flat tensile specimens with nominal dimensions of 9 × 2.7 × 0.5 (mm) in the gauge section. Mechanical grinding and a final electrochemical polishing (50 g CrO₃ in 200 g H₃PO₄) were employed to remove the entire processing-affected surface layer.

The specimens with UFG structure were electrochemically hydrogen-charged (H-charged) at a current density of 10 mA/cm² for $\tau_H = 5, 10, 20, 40, 65,$ and 100 hours at room temperature in 3% NaCl water solution containing 3 g l⁻¹ of NH₄SCN as a recombination poison. The coarse-grained specimens were hydrogen-charged in similar regime for 100 hours.

The tensile tests were conducted at room temperature at an initial strain rate of 1.1×10^{-4} s⁻¹ using an electromechanical machine (LFM-125 from Walter+Bai AG).

After fracture, the side and fracture surfaces were examined with a scanning electron microscope (SEM) Quanta 200 3D.

The microstructures of the specimens were investigated by transmission electron microscopy (TEM) using a Technai G2 FEI and JEM2100 microscopes with an accelerating voltage of 200 kV. The samples for TEM were cut in the form of disks with a diameter ≈ 3 mm in the plain of last pressing-pass. Foils were mechanically thinned to ≈ 150 μ m in thickness and electrolytically polished with a Micron 3M device using an electrolyte of 95 pct glacial acetic + 5 pct perchloric acid. The analysis of the microstructure and dislocation arrangement for hydrogen-saturated specimens was carried out in the near-

Table 1. Chemical composition of the steels (wt. %). Fe-balanced.

Notation	Cr	Ni	Mo	Ti	Mn	Si	Cu	P	S	W	V	C
CrNiMo steel	16.9	13.3	2.7	0.01	1.7	0.6	N/D	0.014	N/D	0.01	0.05	0.01
CrNiTi steel	17.7	9.8	0.2	0.62	1.3	0.5	0.2	0.032	N/D	0.03	0.07	0.11

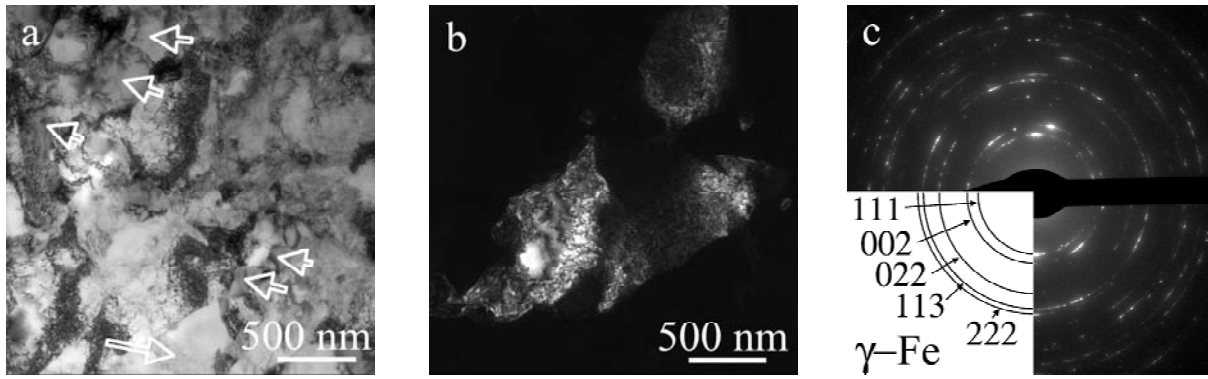


Fig. 1. TEM bright-field (a) and dark-field (b) images, and SAED pattern (c) in UFG-CrNiTi steel. Arrows on the image (a) show dislocation-free grains. SAED pattern corresponds to the image (a) and is obtained from the area of $27 \mu\text{m}^2$.

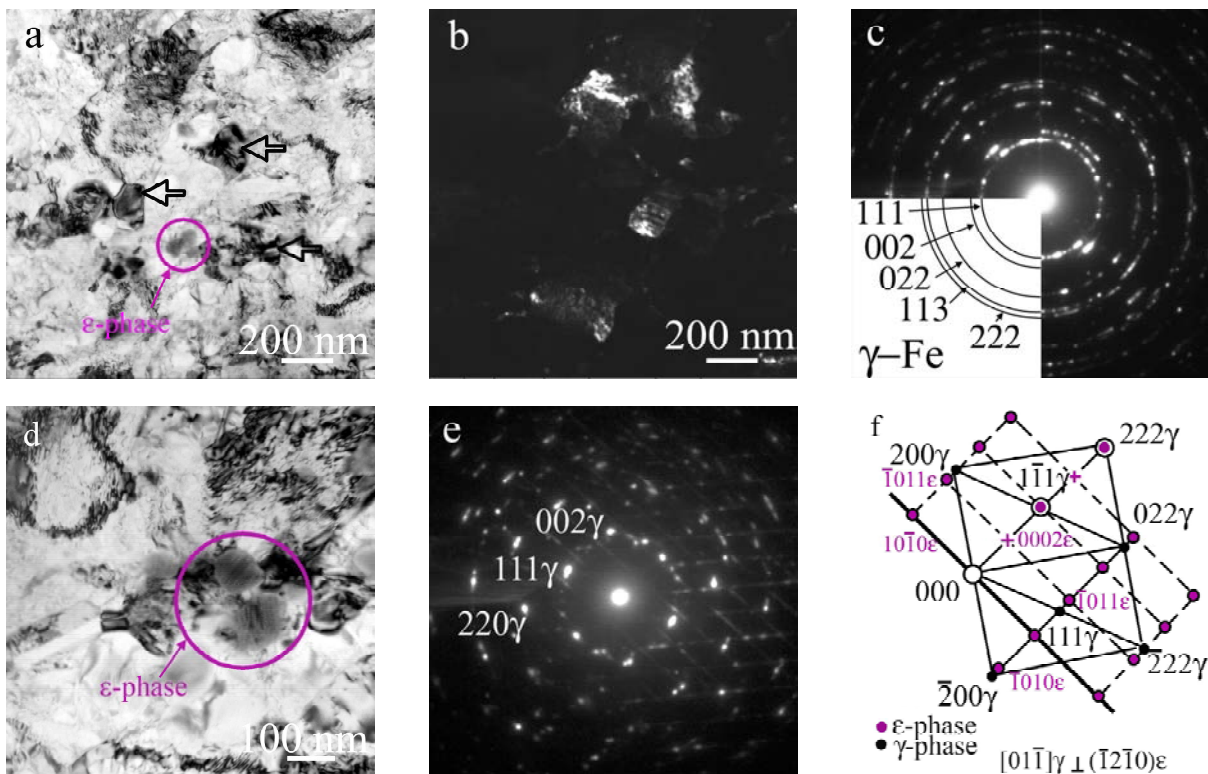


Fig. 2. TEM bright-field (a, d) and dark-field (b) images, SAED pattern (c, e) for UFG-CrNiMo steel. Recrystallized grains are marked by arrows on the image (a). Grains with plates of ϵ -phase are circled on the images (a, d). SAED patterns (c, e) correspond to the images (a, d) and are obtained from the areas of $1.3 \mu\text{m}^2$ and $0.05 \mu\text{m}^2$, respectively. Combined ($\gamma + \epsilon$) spot diffraction pattern on (f) corresponds to SAED pattern (e).

surface layers of about 15-20 μm deep from the specimen surface. The average sizes of the microstructural elements, subgrains (D) and grains (d), were determined using dark-field TEM-images for at least 200 objects. On the basis of these results, (sub)grain size distributions were established. Indexing of selected area electron diffraction (SAED) patterns was performed as detailed elsewhere [26].

3. RESULTS AND DISCUSSION

3.1. Ultrafine-grained structures produced by ABC-pressing

Typical microstructures evolved under ABC-pressing of UFG-CrNiTi and UFG-CrNiMo steels are shown in Figs. 1 and 2. The phase compositions and characteristics of the microstructures are summarized in Table 2.

Table 2. Phase composition and microstructure parameters of the steels prior to hydrogen-charging.

Notation	Thermomechanical treatment regime	Phase composition	Microstructure parameters
UFG-CrNiMo steel	ABC-pressing	Austenite, ϵ -phase (0.3%)	Grain-subgrain structure, $D = 0.20 \pm 0.14 \mu\text{m}$ (austenite subgrain size), $d = 0.11 \pm 0.05 \mu\text{m}$ (austenite recrystallized grains), $d_{\epsilon} = 0.07 \pm 0.03 \mu\text{m}$ (austenite recrystallized grains with ϵ -phase)
CG-CrNiMo steel	Water-quenching	Austenite	Coarse grained structure, average grain size $d = 16.4 \pm 8.9 \mu\text{m}$
UFG-CrNiTi steel	ABC-pressing	Austenite, α' -phase (0.8%)	Grain-subgrain structure, $D = 0.52 \pm 0.14 \mu\text{m}$ (austenite subgrain size), $d = 0.24 \pm 0.17 \mu\text{m}$ (austenite recrystallized grains)
CG-CrNiTi steel	Water-quenching	Austenite	Coarse grained structure, average grain size $d = 31.83 \pm 15.37 \mu\text{m}$

After ABC-pressing, both steels have mainly austenitic structures with rather homogeneous size distributions of grains and subgrains. The mean values for subgrain size (D) lie in submicrometer range for both steels, but for the UFG-CrNiTi steel D is higher (520 nm) than that for UFG-CrNiMo steel (200 nm) (Table 2). Despite similar ABC-pressing regimes, the lower temperature of the last pressing-passes and higher cumulative strain provide smaller subgrain size in UFG-CrNiMo steel compared to UFG-CrNiTi one.

According to TEM bright- and dark-field analysis, the UFG-CrNiTi steel has highly defective structure with both high- and low-angle boundaries and with the high density of dislocations ($\sim 10^{14} \text{ cm}^{-2}$). Dislocations are not uniformly distributed inside of deformed grains and subgrains: areas with dislocation net or with cellular-like dislocation arrangement, dislocation-assisted subboundaries and dislocation tangles next to the grain boundaries are visible. After ABC-pressing, the mean subgrain size is 520 nm as it was measured using dark-field TEM images (Fig. 1b, Table 2). Together with grains and subgrains, which were produced via complex effects of hot-to-warm plastic deformation processes (during ABC-pressing), static (during heating to pressing temperature) and dynamic (during ABC-pressing) recrystallization, a submicrometer-sized ($d=240$ nm, Table 2), dislocation-free grains were also observed (marked by arrows in Fig. 1a). Such grains

rounded by high-angle boundaries arise as a result of recrystallization during the last pressing-pass. This fact confirms the importance of recrystallization processes into ultrafine-grained refinement of the structure during high-temperature plastic deformation, which were earlier shown in [21,27].

The volume fraction of the α' -phase in UFG-CrNiTi specimens is not high (0.8%) because pressing temperatures are higher than the $\gamma \rightarrow \alpha'$ deformation-induced transformation temperature interval in most CrNi steels [28,29].

ABC-pressing facilitates sufficient refinement of the structure in CrNiMo steel. TEM analysis testifies to the formation of complex grain-subgrain structure in CrNiMo steel as a result of high-temperature deformation (Figs. 2a-2c). Structural elements with both high- and low-angle boundaries arise due to high-temperature plastic deformation, such elements contain a high dislocation density similar to UFG-CrNiTi specimens. The temperature of the final pressing-passes $T=600$ °C in CrNiMo steel was 100 °C lower compared to CrNiTi steel. In spite of this fact, dislocation-free recrystallized grains ($d=110$ nm, Table 2) are also present in UFG-CrNiMo steel (marked by arrows in Fig. 2a).

The strain-induced $\gamma \rightarrow \epsilon \rightarrow \alpha'$ and $\gamma \rightarrow \alpha'$ phase transformations are suppressed in this steel due to rather high ABC-pressing temperatures. For this reason, no α' strain-induced martensite was found

in UFG-CrNiMo specimens. Nevertheless, small grains containing thin plates of ε -phase were observed in ABC-processed structure (Figs. 2a and 2d, Table 2). Plates of ε -phase several nanometers thick arise in small grains with the mean size of 70 nm. Such grains are filled with ε -phase plates and contain no or just a few visible dislocations. Probably, strain-induced phase transformation occurs during plastic deformation in small recrystallized grains (produced in previous pressing-pass), which are too small for deformation by dislocation slip. The volume fraction of grains with α -phase is not high (0.3%), therefore, they hardly affect hydrogen-assisted response of the material.

3.2. Tensile plastic flow in UFG steels

Tensile engineering stress - engineering strain curves for hydrogen-free and hydrogen-charged specimens of UFG-CrNiTi and UFG-CrNiMo steels are shown in Figs. 3a and 3b. For comparison, the effect of 100 h hydrogen-charging on stress-strain curves in CG steels are also given in Fig. 3c.

ABC-pressing procures high strength properties in the steels: 0.2% proof stresses for UFG-CrNiTi and UFG-CrNiMo specimens are 3.5-4.5 times higher than that for CG-CrNiTi and CG-CrNiMo counterparts (Fig. 3d). Despite this fact, the elongation to fracture for UFG specimens is sufficiently low compared to coarse-grained steels (Figs. 3a-3c, 3e). The lower (sub)grain size provides higher strength, but very limited plastic properties in UFG-CrNiMo steel (Figs. 3a, 3b, and 3e).

Stress-strain dependence in UFG-CrNiMo specimens looks similar to characteristic plastic flow in steels processed by severe plastic deformation. For such UFG and nanostructured materials, a macroscopic localization occurs after short stage of uniform elongation and plastic deformation is concentrated in such localized bands [30,31]. Macroscopic localization is often accompanied by drop in deforming stress and by negative strain hardening on engineering stress-strain curves [30,31].

Unlike the common features of deformation of UFG steels, UFG-CrNiMo specimens do not undergo the macroscopic localization until strain reaches $\approx 4\%$. This means that UFG-CrNiMo steel possesses uniform deformation in stage corresponded to negative slope of stress-strain dependence (Fig. 3a). At the latter stage $\varepsilon > 4\%$, a macroscopic neck forms and this process proceeds simultaneously with fast decrease in stress.

UFG-CrNiTi specimens demonstrate uniform plastic deformation until the stage of neck forma-

tion at $\varepsilon \approx 8\%$ (Fig. 3b). This uniform elongation corresponds to linear stress-strain dependence. At $\varepsilon > 8\%$, a macroscopic neck forms and stresses decrease until failure occurs.

Hydrogen-saturation up to 100 hours weakly influences stages of plastic flow both in UFG and CG steels (Figs. 3a-3c). But the effect of hydrogen-charging on plastic properties of ultrafine-grained and coarse-grained austenitic steels differs.

The value of 0.2% proof stress ($\sigma_{0.2}$) shows nonlinear dependence on saturation period t_h in case of UFG steels. For UFG-CrNiMo specimens, the stresses $\sigma_{0.2}$, first, grow with hydrogen-charging up to 10 hours and, then, gradually decrease with saturation duration t_h up to 100 hours (Fig. 3d). In case of UFG-CrNiTi, one could check an opposite effect: increase in saturation duration up to $t_h=40$ h facilitates to slow decrease and following increase in $\sigma_{0.2}$ value at longer saturation period (Fig. 3d). For CG-CrNiTi and CG-CrNiMo steels, stress $\sigma_{0.2}$ changes insufficiently with hydrogen-charging for 100 hours (Fig. 3d).

Independently on hydrogen-charging duration, elongation to fracture does not vary with hydrogenation for both steels with UFG structure (Fig. 3e). At the same time, surface hydrogen saturation for 100 hours of coarse-grained CrNiTi steel causes about 10% loss in total elongation of the specimens (Fig. 3e). This experimental data evidences that high density of deformation defect and deformation-induced low- and high-angle boundaries does not provoke hydrogen embrittlement in CrNiTi and CrNiMo steels.

3.3. Microstructure and deformation mechanisms in UFG steels

UFG-FeCrMo steel. The typical microstructures in UFG-CrNiMo steel specimens depending on hydrogen-charging duration are shown in Fig. 4 for two characteristic states: (i) after hydrogen-charging without any plastic deformation (Figs. 4a-4c) and (ii) after hydrogen-charging following by tension to failure (Figs. 4d-4f).

TEM images in Figs. 4a-4c clearly show several hydrogen-assisted effects on ultrafine-grained structure in UFG-CrNiMo steel. First, saturation with hydrogen provokes partial relaxation of highly defective UFG structure produced by ABC-pressing. Bright-field analysis could hardly recognize the difference between hydrogen-free and hydrogen-charged states – complicated diffraction contrast testifies to misoriented structures with high defect density, low- and high-angle boundaries (Figs. 4a-

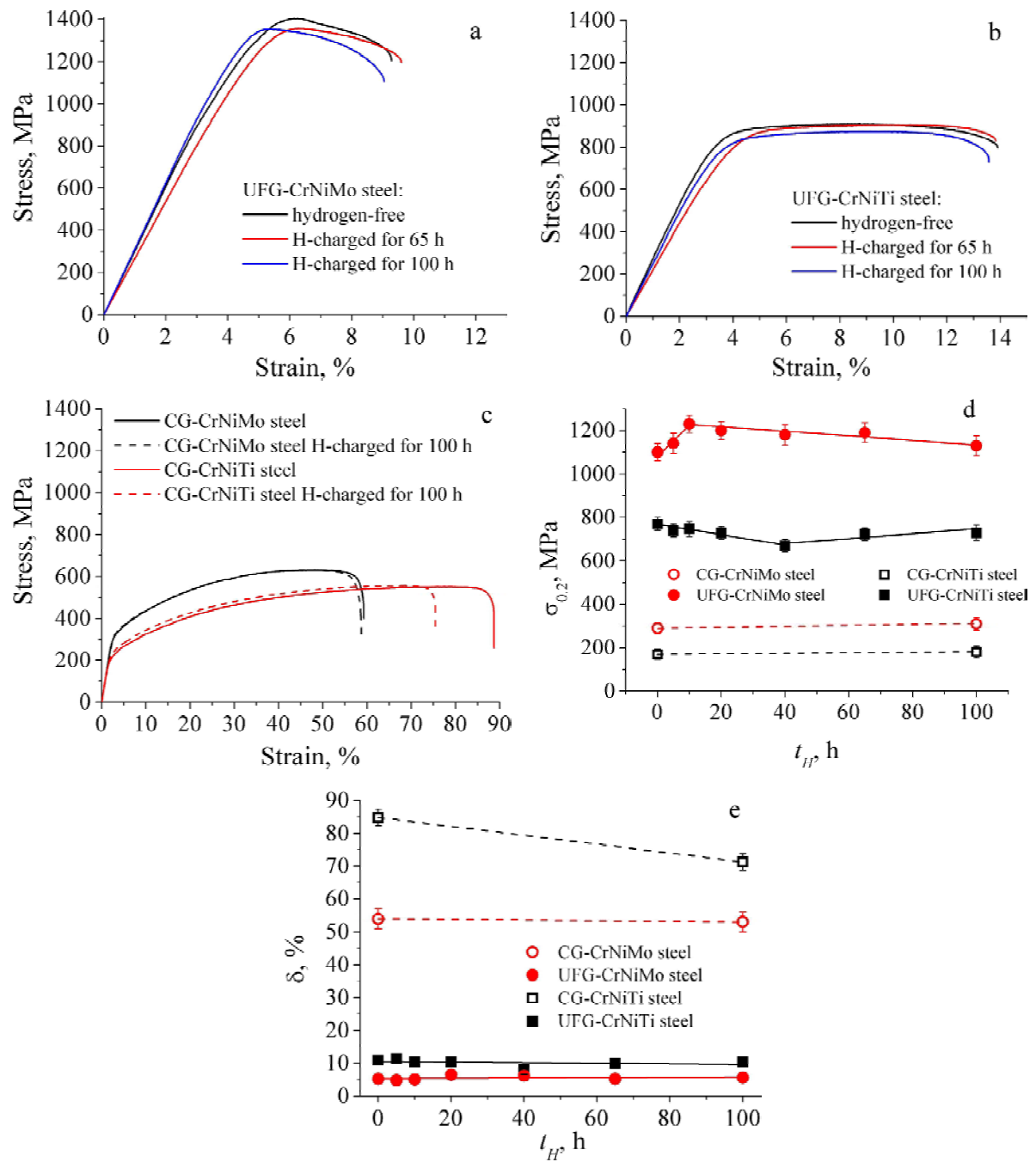


Fig. 3. The effect of hydrogen-charging on engineering stress-engineering strain curves for ultrafine-grained UFG-CrNiMo (a) and UFG-CrNiTi (b) steels and coarse-grained CG-CrNiMo and CG-CrNiTi steels (c) under tension. Data on 0.2% proof stresses (d) and elongation (e) depending on hydrogen-charging duration for ultrafine-grained and coarse-grained steels.

4c). But obvious decrease in azimuthal blurring of the reflections is seen on the SAED patterns corresponded to hydrogen-charged specimens (Figs. 4b and 4c) as compared to hydrogen-free one (Fig. 4a). After 100 h-H-charging SAED pattern has mainly point characteristics, austenite reflections are evenly distributed along the rings. This means that mainly high-angle misorientations characterize the microstructure in Fig. 4c. Therefore, hydrogen alloying

changes the relation between low- and high-angle misorientations in ultrafine-grained structure of UFG-CrNiMo steel and decrease fraction of low-angle misorientations.

In addition to change in SAED pattern, a dark-field analysis shows some variations in subgrain size distributions after hydrogen-charging of UFG-CrNiMo specimens (Figs. 5a and 5c). The fraction of small elements (less than 50 nm) increases two-fold and

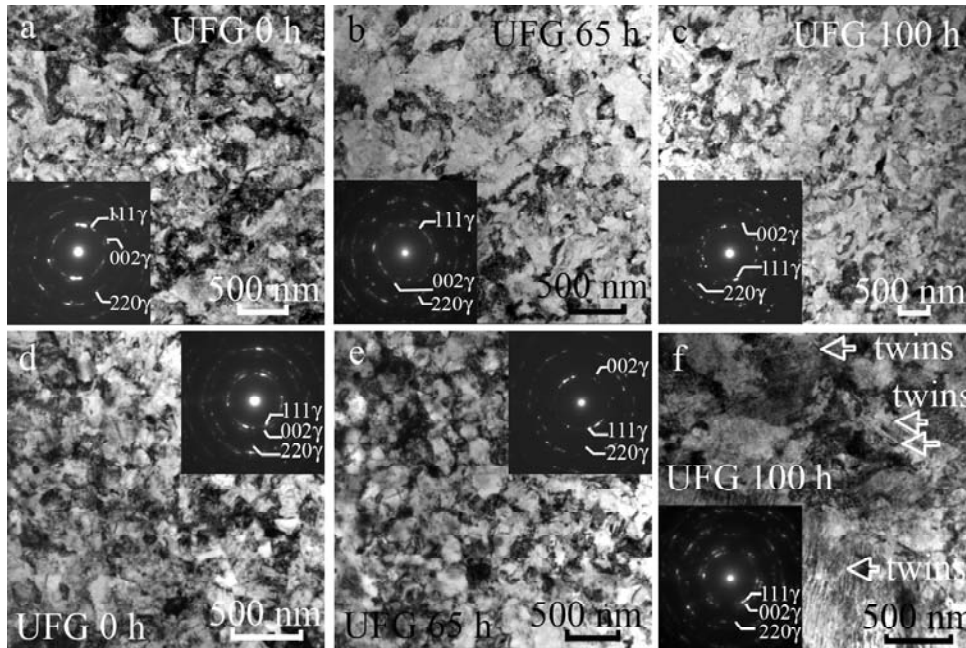


Fig. 4. The characteristic TEM bright-field micrographs and SAED patterns (inserted) in UFG-CrNiMo steel depending on hydrogen-charging regime and strain: a, b, c – specimens H-charged after ABC-pressing; d, e, f – specimens H-charged after ABC-pressing and deformed in tension to fracture. a, d – hydrogen-free specimen; b, e – hydrogen-charged for 65 hours; c, f – hydrogen-charged for 100 hours. SAED patterns is obtained from the area of $27 \mu\text{m}^2$. TEM images correspond to surface hydrogen-saturated layers.

the most probable size shifts from 50-100 nm to 150-200 nm range (Fig. 5c). At the same time, the width of distribution does not change and fraction of large elements (larger than 400 nm) decreases. Such behavior could be associated with hydrogen-induced redistribution of dislocations in UFG steels. Hydrogen-assisted dislocation migration in UFG structure, which always possesses high internal stresses [31,32], can occur both in subgrain bodies and near boundaries because hydrogen increases the mobility of dislocations [9,33-35] due to shielding their elastic fields. From the one side, this could slightly increase the mean subgrain size due to disintegration of dislocation walls or redistribution of dislocations near boundaries. This, in turn, can increase the fraction of high-angle boundaries. From the other side, rearrangement of dislocations could cause formation of new small subgrains or cells (Figs. 6a and 6b) similar to recovery process [36]. Shyvanyuk et al. [37] noticed hydrogen-associated decrease in recrystallization temperature in pre-strained 304 stainless steel, which was related to the enhanced diffusion of host atoms because of hydrogen-induced increase in the thermodynamic equilibrium concentration of vacancies. The complex impact of these factors could be the reason for slight increasing of sizes of former subgrains and changing the characteristics of their boundaries.

One more hydrogen-assisted effect is increase in fraction of small grains filled with ε -martensite (Figs. 6a and 6b). The mean size of such grains, as it was measured using TEM images, is 43 nm and 54 nm after 65 and 100 hours of H-charging respectively. These sizes are even smaller than that for ABC-pressed specimens (70 nm). The possible explanation for formation of such grains is that $\gamma \rightarrow \varepsilon$ transformation acts as stress-relaxation mechanism in very fine grains, where dislocation sources do not work.

In tension of hydrogen-free UFG-CrNiMo specimens, dislocation slip is the main deformation mechanism (Fig. 4d). As it realizes in highly defective and refined structure, tensile plastic deformation is accompanied by slight increase of the subgrain size. Such behavior is a result of concurrent processes – deformation-associated defect accumulation (refinement) and strain-induced defect relaxation (coarsening) (Fig. 5b). Subgrain coarsening interprets data on negative slope of stress-strain curve during stage of uniform elongation (Fig. 3a). Hydrogen-charging further stimulate the coarsening of the structural elements during tension, as it was revealed by TEM analysis (Figs. 4e, 4f, and 5d). According to Fig. 5d, the fraction of elements with sizes less than 200 nm decreases twice, and new maximum forms in subgrain size range 400-800 nm.

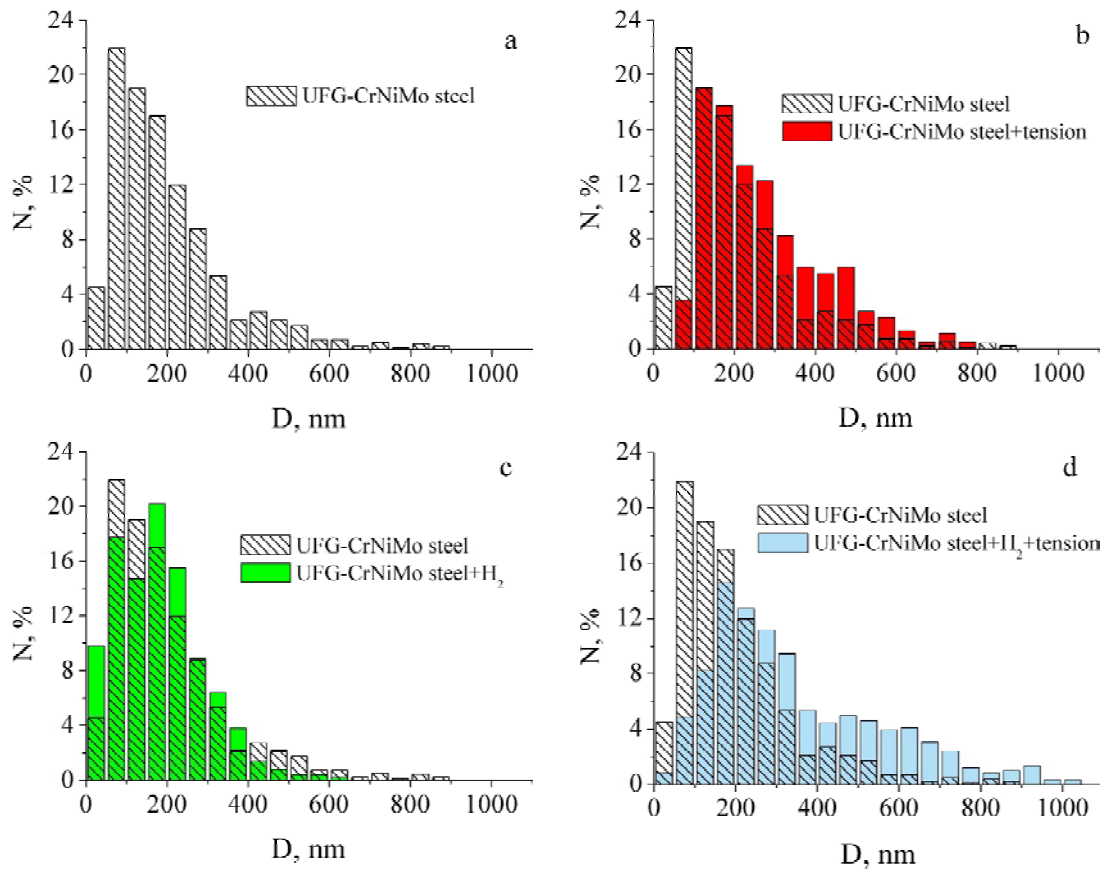


Fig. 5. Comparison of the (sub)grain size distributions in UFG-CrNiMo steel after different treatment regimes: a – initial state (as-ABC-pressed); b – combined diagrams for initial state and initial state + tension; c – combined diagrams for initial state and initial state + hydrogen charging for 100 hours; d – combined diagrams for initial state and initial state + hydrogen charging for 100 hours + tension to fracture.

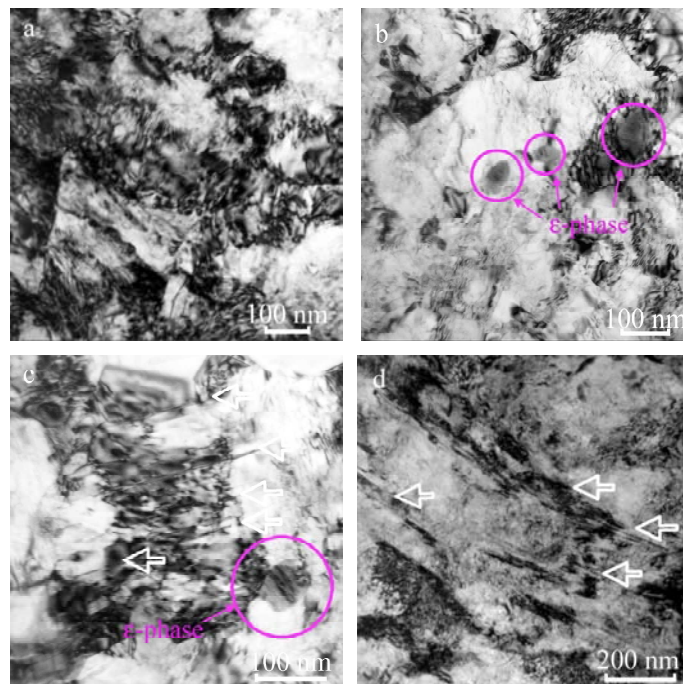


Fig. 6. Details of the microstructure in UFG-CrNiMo steel specimens: a – after ABC-pressing; b – after ABC-pressing and H-charging for 65 hours; c – after ABC-pressing, H-charging for 65 hours and tension; d – after ABC-pressing, H-charging for 100 hours and tension. Arrows on images (c) and (d) show mechanical twins. All images correspond to surface hydrogen-saturated layers.

Together with subgrain size variation and increase in fraction of high-angle boundaries, hydrogen-charging changes deformation mechanisms in CrNiMo steel. Hydrogen alloying promotes to deformation twinning (Figs. 6c and 6d). For instance, after 100-hours hydrogen-charging, subgrains with plates of twins are seen on TEM images (Figs. 4f, 6c, and 6d). Nevertheless, dislocation slip dominates in hydrogen-charged UFG-CrNiMo specimens in tension.

UFG-FeCrTi steel. The initial subgrain size in this steel as-processed by ABC-pressing was about half of micrometer. Hydrogen-charging causes partial relaxation and coarsening of the UFG structure similar to hydrogenation effect in UFG-CrNiMo steel. SAED patterns tend to have point characteristics with low azimuth spreadings in H-contained specimens (Figs. 7a-7c). After 100 h-charging with hydrogen, the average subgrain size increases up to 590 ± 20 nm (520 nm in hydrogen-free steel) and subgrain size distribution shifted to the larger element size compared to H-free state (Figs. 8a and 8c). TEM analysis of the H-charged specimens shows 100-300 nm austenitic regions (cell-like) bounded with dislocation tangles. Such cells possess rather homogeneous contrast, which demonstrate partial annihilation or rearrangement of dislocations into dislocation tangles as a result of hydrogen-charging (Figs. 9a and 9b). Wide stacking faults, splitted dislocations and low density of perfect dislocations are evaluated in the bodies of this cells (Fig. 9b). The borders of the cells, dislocation tangles, do not procure high-angle boundaries between neighboring elements, but provide discrete low-angle misorientation between them. Such cellular-like configuration with low-angle discrete boundaries manifests point characteristics of the SAED patterns in hydrogen-charged UFG steels (Fig. 7c). While, continuous low-angle misorientations associated with high dislocation density and internal stresses in severely deformed hydrogen-free UFG-CrNiMo and UFG-CrNiTi steels provided high azimuthal diffusion on SAED patterns (Figs. 4a and 7a).

During tension of UFG-CrNiTi steel specimens, plastic deformation realizes due to dislocation slip and mechanical twinning (Fig. 7d). Twin lamellae of several micrometers long extend through subgrains, stop or change the direction of their distribution on boundaries (Fig. 7d). Both mechanisms, slip and twinning, act as hardening factors during plastic deformation. The size-distribution of the subgrains show insignificant change after tension compared to initial UFG-state produced by ABC-pressing. Similar to UFG-CrNiMo, tension of hydrogen-free ultrafine grain-subgrain structure is accompanied

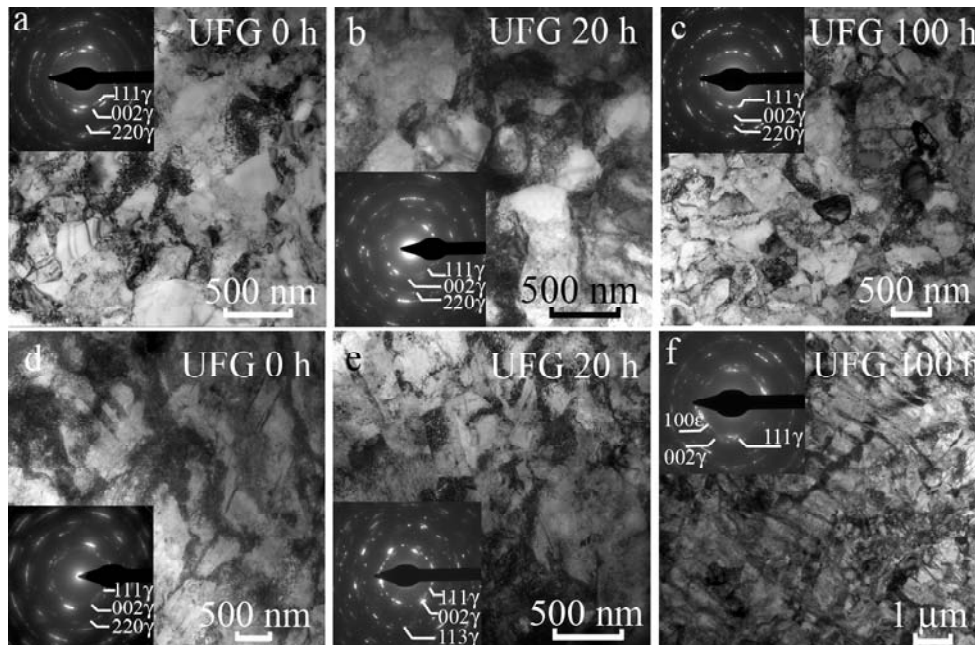


Fig. 7. The characteristic TEM bright-field micrographs and SAED patterns (inserted) in UFG-CrNiTi steel depending on hydrogen-charging regime and strain: a, d – hydrogen-free specimen; b, e – hydrogen-charged for 20 hours; c, f – hydrogen-charged for 100 hours; a, b, c – specimens after ABC-pressing; d, e, f – specimens after ABC-pressing and tension to fracture. SAED patterns is obtained from the area of $27 \mu\text{m}^2$. TEM images correspond to surface hydrogen-saturated layers.

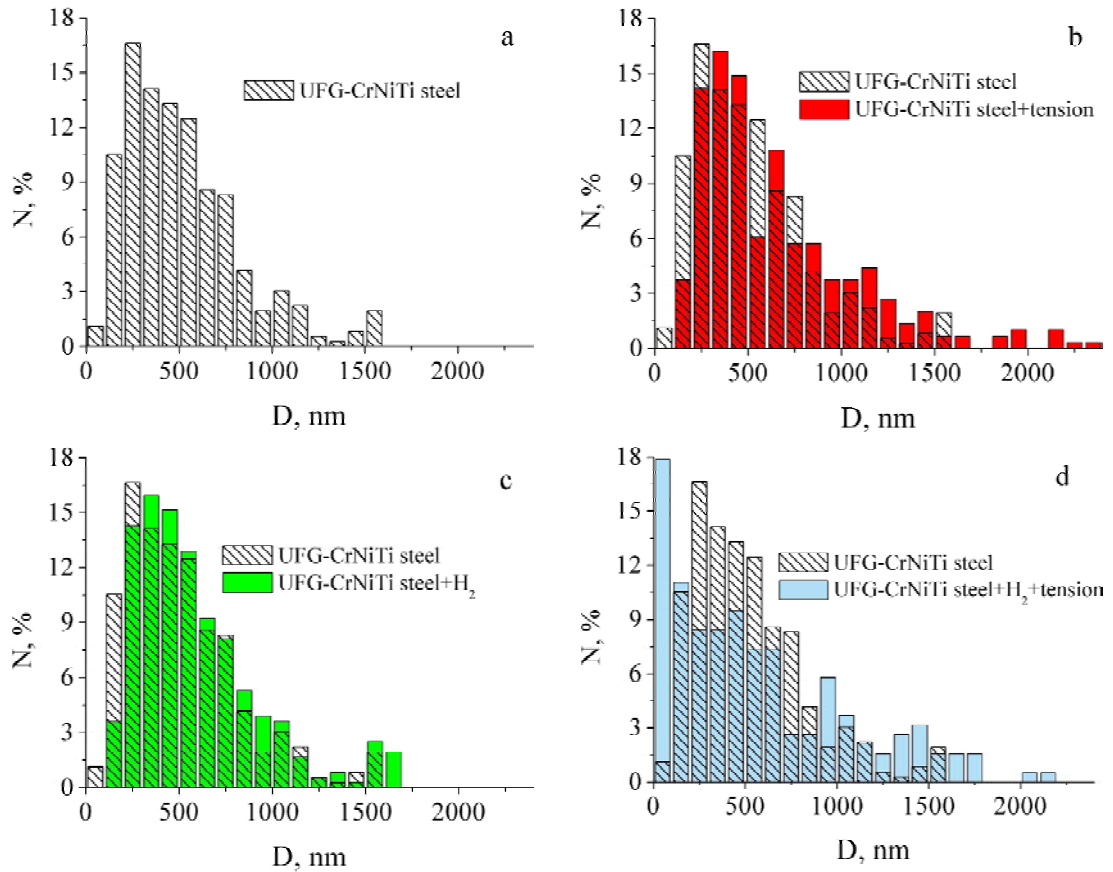


Fig. 8. Comparison of the (sub)grain size distributions in UFG-CrNiTi steel after different treatments: a – initial state (as-ABC-pressed); b – combined diagrams for initial state and initial state + tension; c – combined diagrams for initial state and initial state + hydrogen charging for 100 hours; d – combined diagrams for initial state and initial state + hydrogen charging for 100 hours + tension to fracture.

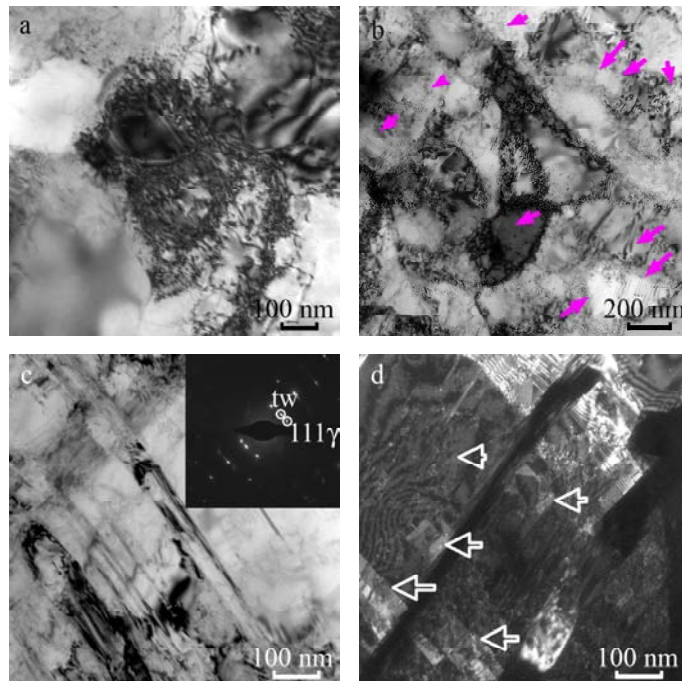


Fig. 9. Details of the microstructure in UFG-CrNiTi steel specimens: a – after ABC-pressing; b – after ABC-pressing and H-charging for 100 hours; c, d – after ABC-pressing, H-charging for 100 hours and tension. Arrows on images (b) and (d) show stacking faults. All images correspond to surface hydrogen-saturated layers.

with slight increase in subgrain sizes (softening mechanism). Complex effect of softening and hardening mechanisms during tensile deformation provides uniform and rather high deformation in specimens of UFG-CrNiTi steel.

Hydrogen-charging promotes twinning and $\gamma \rightarrow \varepsilon$ transformation in UFG-CrNiTi steel. These deformation mechanisms realize in most of the grains (Figs. 7e, 7f, 9c, and 9d). Twin or ε -martensite lamellae are clearly seen in TEM images, and SAED patterns contain characteristic spreadings and streaks, which testify to low thickness of lamellae (Figs. 7f and 9c). Together with twins or ε -martensite lamellae, microtwins, and stacking-faults are characteristic features of the structure of H-charged and deformed specimens (Fig. 9d). Twin and ε -martensite boundaries divide subgrains into smaller domains, so the fraction of small-size fragment increases in grain-size distribution in Fig. 8d. According to data of magnetic-phase analysis, the fraction of α' -martensite increases from 0.8% up to 2.0% as a result of tensile deformation in hydrogen-free specimens, and up to 1.3% in hydrogen-charged one. These variations in volume fraction of deformation-induced martensite is one order of experimental error, and they need an additional confirmation.

3.4. Hydrogen-assisted twinning and deformation-induced martensitic transformation

Twinning and deformation-induced martensitic transformations are SFE-dependent deformation mechanisms [29,38]. CrNiTi and CrNiMo steels before hydrogen-charging possess different SFE due to difference in chemical compositions. Several empirical relations were proposed for the estimation of SFE [2]. According to Rhodes [39] relation, the SFEs are about 35 mJ/m² for CrNiMo steel and 24 mJ/m² for CrNiTi steel. Padilha [40] summarized data on SFE of different authors and gave rather high interval of SFE for the steels in conventional CG state: 35-81 mJ/m² for CrNiMo steel and 15-42 mJ/m² for CrNiTi steel. Nevertheless, all data testify to higher SFE and more stable austenitic structure in CrNiMo steel compared to CrNiTi one.

Another important factors, responsible for austenite stability against martensitic transformation, are M_s and M_d temperatures (start temperature for martensitic transformation under cooling and limit temperature of deformation-induced martensite formation). In the temperature interval between M_s and M_d the deformation-induced martensite forms (strain- and stress-induced) [29]. For the most of conven-

tional Cr-Ni steels, M_s temperature lies below room temperature. For instance, the characteristic temperatures for Fe-19Cr-11Ni steel are $M_s \approx -75$ °C and $M_d \approx 130$ °C [29], and $M_s \approx -100$ °C, and $M_d \approx 150$ °C for Fe-18Cr-10Ni steel [41]. We estimated M_s temperatures based on chemical composition of our steels [2]: $M_s \approx 60-75$ °C for CrNiMo steel and $M_s \approx 90-100$ °C for CrNiTi steel. These values are overestimated because both steels possess austenitic structure at room temperature. But estimated parameters testify to different stability of the CrNiTi and CrNiMo steels to deformation-induced phase transformation. They also show that M_s temperature for CrNiMo steel is lower than that for CrNiTi one, which determines higher CrNiMo austenite stability against phase transformations.

Aforementioned differences in SFE and M_s temperature are responsible for different deformation mechanisms in CG steels in tension at room temperature: mainly dislocation slip in CrNiMo steel [23, 42] and combination of slip, twinning and $\gamma \rightarrow \alpha'$ phase transformations in CrNiTi steel [23, 25]. Steels with UFG structures behave in absolute accordance with CG steels: pronounced mechanical twinning was observed in TEM images corresponded to deformed specimens of the UFG-CrNiTi steel possessing lower SFE; dislocation slip dominated in UFG-CrNiMo steel possessing higher SFE (Figs. 4d and 7d). Decrease in grain size and limitation of plasticity in UFG steels both suppress deformation-induced phase transformation [24,28]. For this reason, the volume fraction of α' -martensite insignificantly increases in UFG-CrNiTi steel during tension.

Hydrogen decreases SFE of the steels and promotes planarity of dislocation structure, twinning and $\gamma \rightarrow \varepsilon$ martensitic transformation [34,43-45]. All these effects are associated with the splitting of the perfect slip dislocations $a/2\langle 110 \rangle$ on partial Shockley dislocations $a/6\langle 211 \rangle$ separated by stacking fault ribbons, emission on partials from grain boundaries, grain boundary splitting, etc. [46].

For austenitic steels, nucleation of twin and ε -martensite occurs by regular superposition of stacking faults on each or every second $\{111\}$ closely packed planes, respectively [29,38]. Therefore, both these mechanisms are strongly dependent on SFE. Hydrogen-enhanced twinning activity and formation of ε -martensite under tension for both hydrogen-saturated UFG steels gives a corroboration for hydrogen-assisted decrease in SFE, which earlier was confirmed only for CG materials [38]. Detailed TEM examination testify to the mechanism of twin growth by overlapping of the stacking fault ribbons. But the mechanism of stacking fault nucleation in our UFG

steels is unclear both in case of hydrogen-charging without applied stress (Fig. 9b) and in tension of hydrogen-free and hydrogen-charged specimens (Figs. 6c, 6d, 9c, and 9d). Stacking faults often start (or stopped) on boundaries, but also are visible in grain bodies (Figs. 9b and 9d), so they can nucleate by splitting of perfect dislocations or by emission from grain boundaries as it was shown for UFG materials earlier [46].

Intersection of twin lamellae on conjugative shear systems and/or ϵ -martensite lamellae all are precursors for α' -martensite formation [29]. For this reason, hydrogen-charging acts as parameter promoting to deformation-induced phase transformations. Decrease in grain size has an opposite effect because grain refinement decreases M_s -temperature for $\gamma \rightarrow \alpha'$ martensitic transformation in Cr-Ni steels [24, 28]. Unfortunately, a change in fraction of α' -martensite is too low during tension, so any conclusions on effects of H-assisted increase in SFE and decrease in grain size in UFG-CrNiTi steel is speculative.

3.5. Hydrogen-assisted surface fracture mechanisms in UFG steels

After tensile testing, the side surface and fracture surface of each specimen were examined to evaluate the mechanism of fracture. Figs. 10 to 15 show the characteristic SEM images. The main

micromechanisms of fracture and width of the hydrogen-assisted surface layers in ultrafine-grained CrNiTi and CrNiMo steels are summarized in Table 3.

Ductile dimple rupture with microvoid coalescence is the main fracture mechanism in hydrogen-free steels independently on grain size (Figs. 10a, 12a, 13a, 14a, and 14e). The difference in fracture micromechanisms for UFG and CG steels is in dimple size, which is larger for CG specimens (see, e.g., Figs. 14a and 14d). In UFG specimens, the dimples are larger than the respective subgrain sizes. This result is in the line with data of other authors [47, 48].

The fracture surfaces obtained from UFG-CrNiMo specimens after different hydrogen-charging exposure and tensile tests and from CG-CrNiMo specimens after 100 h-charging and tensile test to fracture are demonstrated in Fig. 10. Independently on hydrogen-charging regime, the UFG-CrNiMo steel fractured in ductile manner. Side surfaces of UFG-CrNiMo specimens (H-charged and fractured) are featureless without any localized regions or surface cracking (Figs. 11a-11f). Detailed SEM examination revealed very thin brittle layers on fracture surfaces of UFG-CrNiMo hydrogen-charged for 5, 10, and 20 hours (Table 3). These layers demonstrate transgranular cleavage fracture (marked as I on Fig. 12b). The width of such layers is about 1-2 μm and it decreases with charging duration (Table 3). Such behavior can be associated with very inhomogeneous

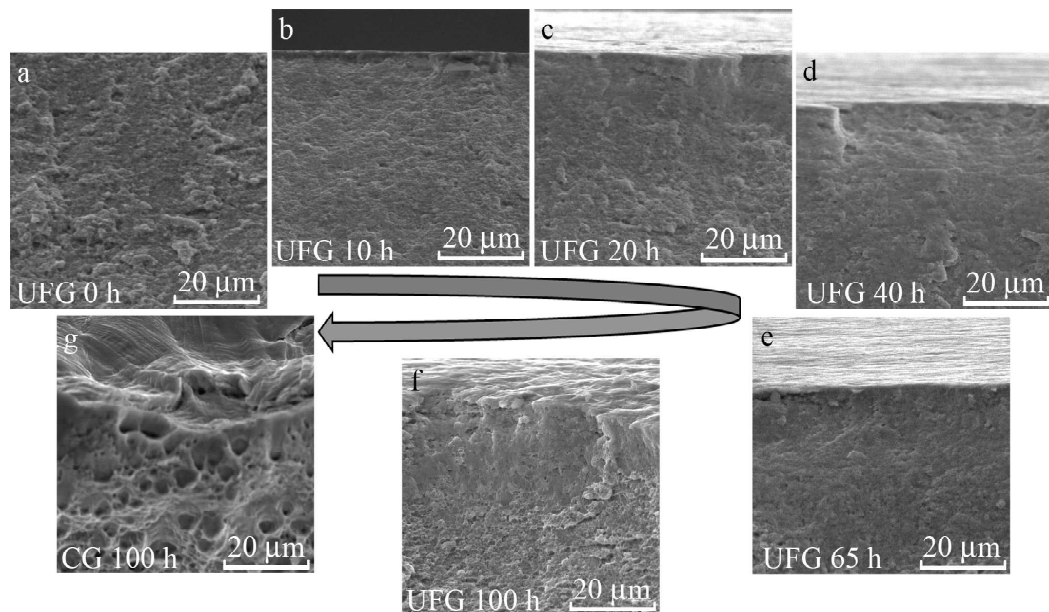


Fig. 10. The characteristic SEM micrographs of the fracture surfaces in UFG-CrNiMo steel depending on hydrogen-charging regime (a-f) and in CG-CrNiMo steel after 100 h-hydrogen-charging (g). One side of the fracture surface is presented for each specimen on images (b)-(g).

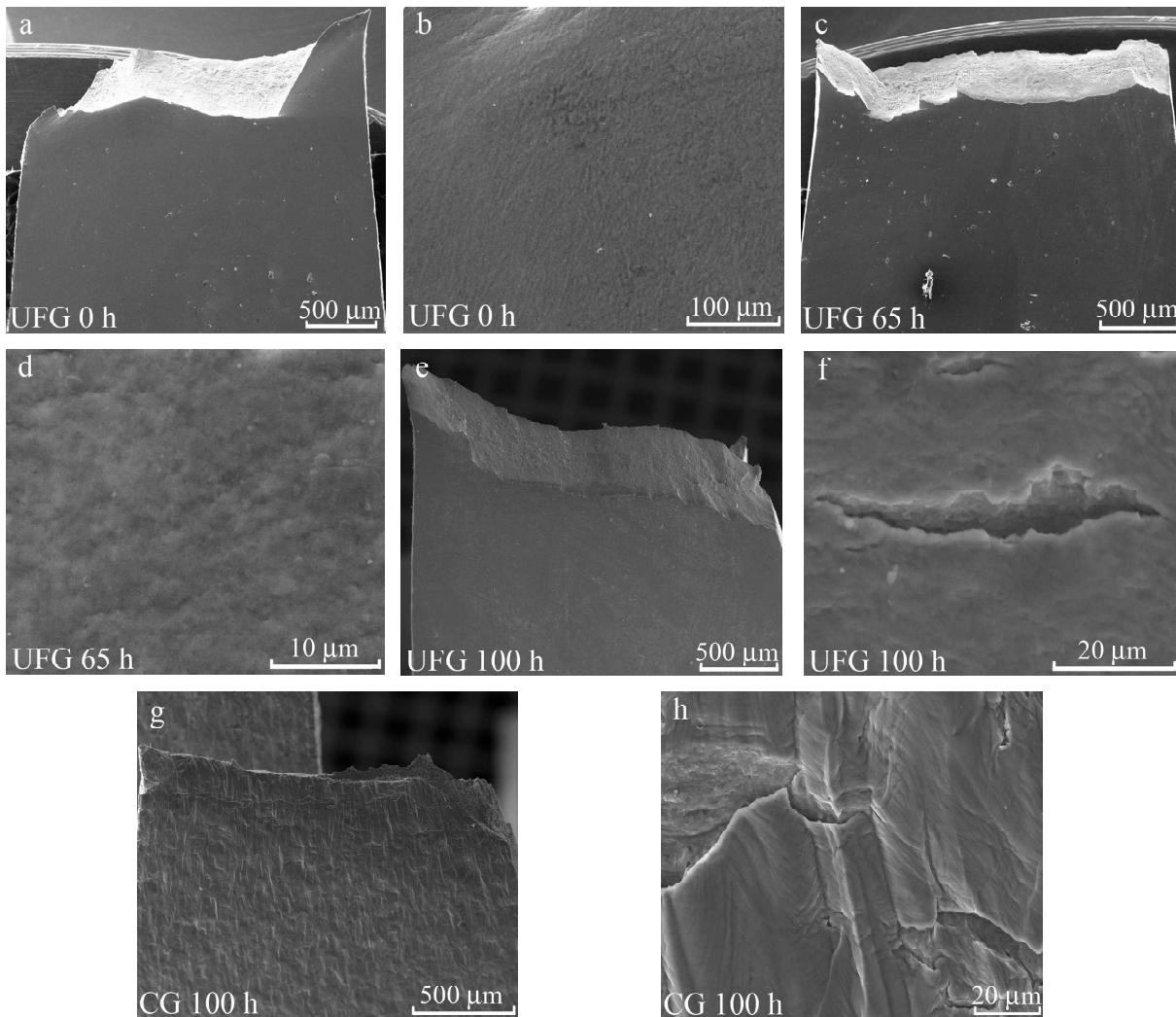


Fig. 11. SEM micrographs of the side-surfaces of the UFG-CrNiMo (a-f) and CG-CrNiMo (g, h) steel specimens depending on hydrogen-charging regime: a, b – hydrogen-free, c, d – hydrogen-charged for 65 hours, e-h – hydrogen-charged for 100 hours. Images (b, d, f, h) are magnified elements of the images (a, c, e, g) obtained near the fracture zones.

ous distribution of hydrogen being diffused into the surface layers of material in 5-20 hours. After longer exposure (65 and 100 hours), brittle surface layers were not detected, but secondary ductile cracks were observed instead (Fig. 12d). Hydrogen effect appears in variation of dimple morphology on fracture surface – elongated and shallow dimples are visible in narrow hydrogen-assisted surface zones (Fig. 12e). Except for this feature, hydrogen-affected surface layers could be hardly identified for UFG-CrNiMo specimens.

Koyama et al. [42] show that for $\langle 001 \rangle$ single crystals of 316 austenitic steel under tensile testing, fracture surface is smooth and mainly ductile. Only a small amount of hydrogen-assisted deformation twin appears in $\langle 001 \rangle$ crystals, and slip is dominating deformation mechanism under tension.

In similar way, hydrogen-saturated surface layers of the UFG-CrNiMo specimens show dimple fracture (Figs. 12c-12e). Smaller, shallower dimples on fracture surface in H-affected zones of UFG-CrNiMo specimens compared to H-free specimens (or in central part of H-charged one) evidence for HELP or combination of HELP and AIDE-assisted fracture mechanisms [10] in slip-controlled deformation of UFG-CrNiMo steel. Elongated dimples also testify to slip localization processes. San Marchi [3] described that elongated dimples is attributed to void nucleating due to the intersection of deformation microbands in hydrogen-containing steels.

According to fractography criterion, UFG-CrNiMo specimens are less prone to HE in comparison with CG analogues. Despite low effect of hydrogen on tensile elongation (Fig. 3e), the cracking of side

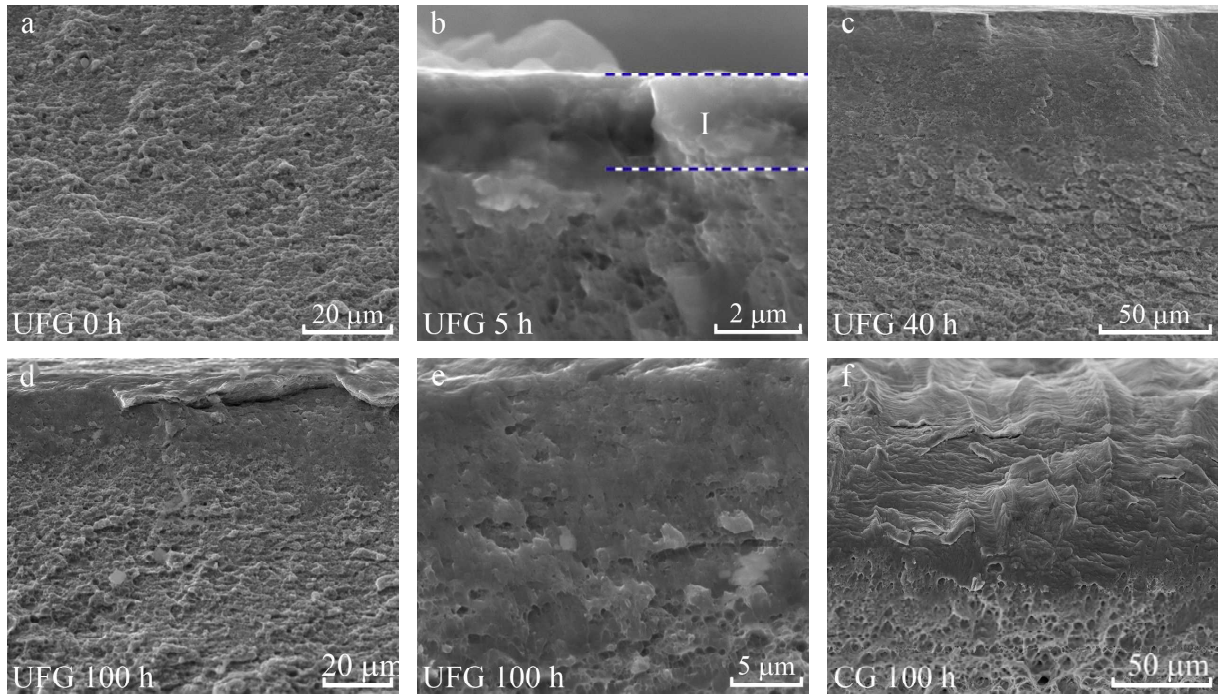


Fig. 12. SEM micrographs of the fracture surfaces of the UFG-CrNiMo (a-e) and CG-CrNiMo (f) steel specimens depending on hydrogen-charging duration: a – hydrogen-free, b – hydrogen-charged for 5 hours, c – hydrogen-charged for 40 hours, d, e, f – hydrogen-charged for 100 hours. Image (e) is magnified element of the near surface area on image (d).

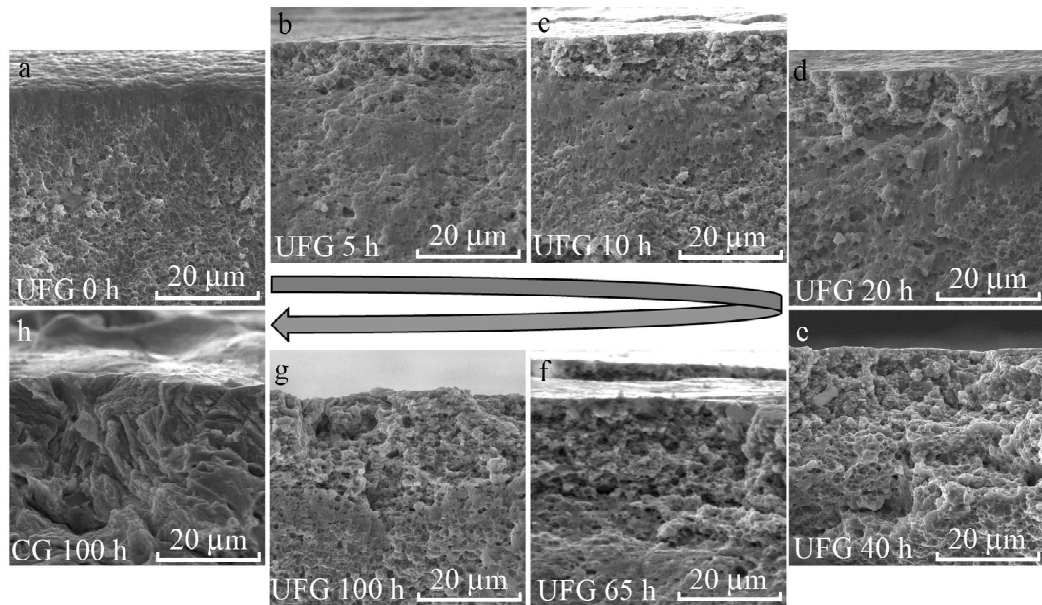


Fig. 13. The characteristic SEM micrographs of the fracture surfaces in UFG-CrNiTi steel in dependence on hydrogen-charging duration (a–g) and in CG-CrNiTi steel after 100h-hydrogen-charging (h). One side of the fracture surface is presented for each specimen on images (a)-(h).

surfaces occurs, and secondary cracks are visible on fracture surface of CG-CrNiMo specimens after deformation in hydrogen-charged state (Figs. 11g, 11h, and 12f). Side-surface images testify to slip-band fracture mechanism in CG specimens [10].

The fracture surfaces obtained from UFG-CrNiTi specimens after H-charging and tensile tests are different from those for UFG-CrNiMo specimens. A typical ductile fracture with microvoid coalescence is characteristic for central parts of the hydrogen-

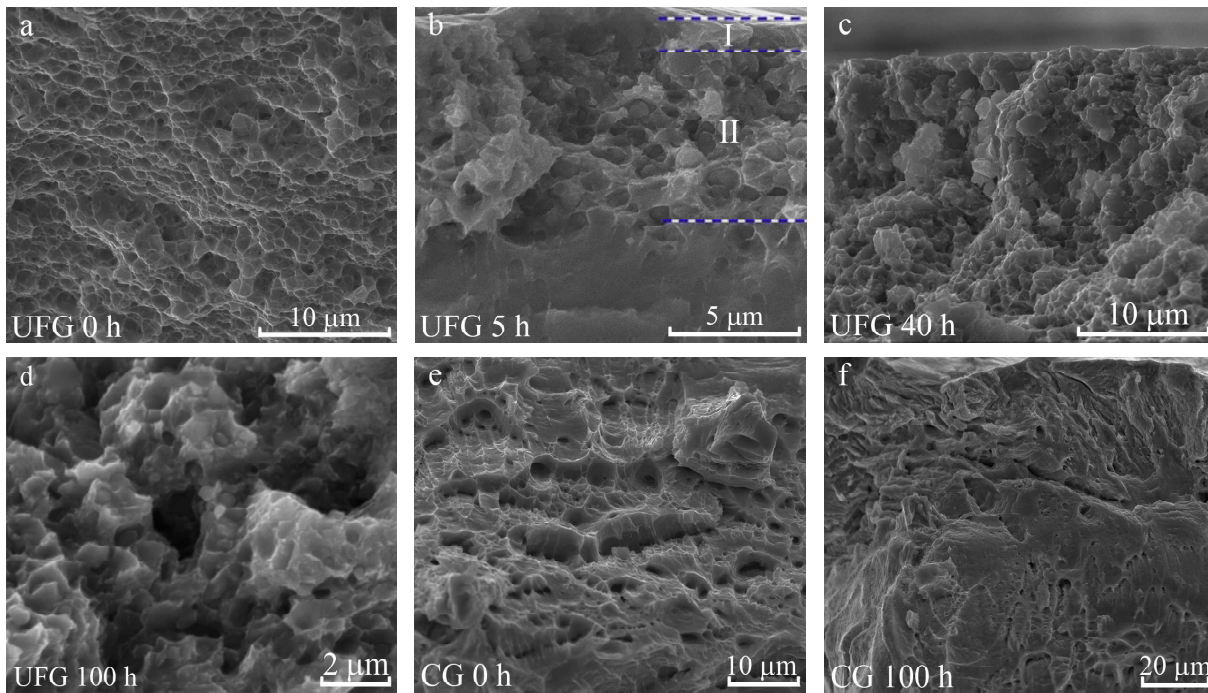


Fig. 14. SEM micrographs of the fracture surfaces of the UFG-CrNiTi (a-d) and CG-CrNiTi (e, f) steel specimens depending on hydrogen-charging duration: a, e – hydrogen-free, b – hydrogen-charged for 5 hours, c – hydrogen-charged for 40 hours, d, f – hydrogen-charged for 100 hours.

Table 3. Micromechanisms of fracture and width of the hydrogen-assisted surface layers in ultrafine-grained CrNiTi and CrNiMo steels.

Steel	Hydrogen-charging duration	Surface brittle layer [μm]	
		I	II
UFG-CrNiTi	hydrogen-free	Not detected	
	5 hours	1.15 \pm 0.11; Transgranular brittle fracture, cleavage mode	7.04 \pm 2.25; Mixed brittle fracture: cleavage transgranular mode (facets $S=1.16 \mu\text{m}$), intergranular mode.
	10 hours	1.13 \pm 0.26; Transgranular brittle fracture, cleavage mode	8.24 \pm 2.75; Mixed brittle fracture: cleavage transgranular mode (facets $S=1.19 \mu\text{m}$), intergranular mode.
	20 hours	0.97 \pm 0.18; Transgranular brittle fracture, cleavage mode	8.74 \pm 0.82; Transgranular brittle fracture, cleavage mode (facets $S = 1.15 \mu\text{m}$)
	40 hours	18.11 \pm 4.67; Transgranular brittle fracture, cleavage mode (facets $S = 1.26 \mu\text{m}$)	
	65 hours	20.66 \pm 3.97; Transgranular brittle fracture, cleavage mode (facets $S = 0.66 \mu\text{m}$)	
	100 hours	20.33 \pm 2.79; Transgranular brittle fracture, cleavage mode (facets $S = 0.72 \mu\text{m}$)	
CG-CrNiTi	100 hours	27.74 \pm 6.20; Transgranular brittle fracture, cleavage mode	
UFG-CrNiMo	hydrogen-free	Not detected	
	5 hours	1.88 \pm 0.41; Transgranular brittle fracture, cleavage mode	Not detected

CG-CrNiMo 1	20 hours	1.04±0.23; Transgranular brittle fracture, cleavage mode	Not detected
	40 hours	0.78±0.11; Transgranular brittle fracture, cleavage mode	Not detected
	65 hours		Not detected
	100 hours		Not detected
	00 hours		Not detected

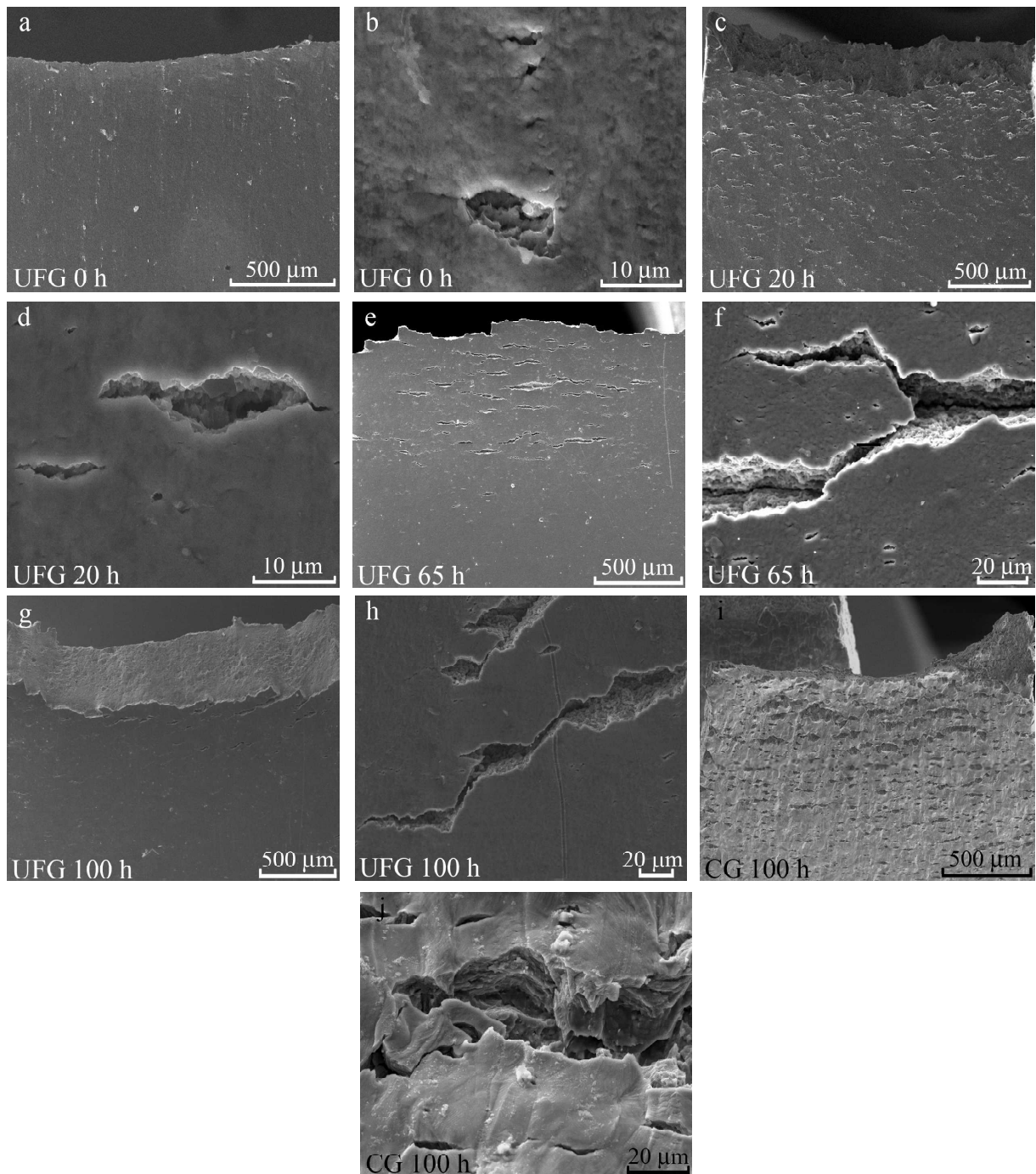


Fig. 15. SEM micrographs of the side-surfaces of the UFGCrNiTi (a-h) and CG-CrNiTi (i, j) steel specimens depending on hydrogen-charging duration: a, b – hydrogen-free, c, d – hydrogen-charged for 20 hours, e, f – hydrogen-charged for 65 hours, g-j – hydrogen-charged for 100 hours. Images (b, d, f, h, j) are magnified elements of the images (a, c, e, g, i) obtained near the fracture zones.

charged UFG-CrNiTi specimens. Hydrogen-assisted brittle surface layers can be easily distinguished on both sides of the fractures (Figs. 13b - 13g). Their widths and fracture micromechanism depend on hydrogenation duration.

For short periods of hydrogen-saturation (5, 10, and 20 hours), brittle fracture zones can be divided into two characteristic regions. The first one, very thin surface layers with transgranular cleavage fracture, are observed, which are similar to those found in UFG-CrNiMo steel (regions I in Figs. 12b and 14b). The second one, region II in Fig. 14b, is much wider than region I, but fractured in brittle mode as well. For hydrogen-charging duration longer than 20 hours, the region I was not observed (as it was also found for UFG-CrNiMo specimens), and brittle surface layers have rather homogeneous relief on fracture surfaces (Figs. 14c and 14d).

The micromechanism of the fracture in brittle hydrogen-assisted layers of UFG-CrNiTi steel changes with hydrogen-charging regime. For specimens tensile tested after 5-20 hours of charging, this layer possesses mixed transgranular and intergranular brittle fracture mainly. But some elements of transgranular dimple fracture also exist even at hydrogen-charging duration for 5 h (Fig. 14b). With increase in H-saturation duration, a transgranular cleavage-like fracture prevails (Figs. 14b-14d, Table 3). Unlike extended regions of quasi-cleavage fracture in CG specimens (Fig. 14f), plane facets (cleavages) in hydrogen-assisted layers of UFG-CrNiTi specimens has very limited sizes (Table 3). The mean size of such facets (S) is one order of value with subgrain sized in UFG-CrNiTi steel and they look like individual transgranular cleavages in ultrafine grains or subgrains (Tables 2 and 3).

The numerous surface cracking occurs under tension of UFG-CrNiTi specimens H-pre-charged for 20 hours (Figs. 15c and 15d). Increase in hydrogenation duration suppresses surface cracking of the UFG specimens under tensile deformation (Fig. 15e-15h). So, after 100 h-precharging, only few surface cracks were formed on side surface of UFG-CrNiTi specimens. While, CG specimens H-charged for 100 h show well-developed surface cracking under tensile testing (Fig. 15i and 15j), which is accompanied by loss in elongation compared to H-free state (Fig. 3e). Hence, UFG-CrNiTi specimens are stable against HE effect in comparison with CG-CrNiTi steel.

TEM data on microstructure of hydrogen-saturated specimens during tension testify to increasing contribution of mechanical twinning and ε -martensite in plastic deformation of hydrogen-satu-

rated surface layers. It is reasonable to assume that change in micromechanism of hydrogen-assisted fracture with long saturation regime is associated with crack formation along twin boundaries or austenite/ ε -martensite interfaces in UFG-CrNiTi steel. Koyama et al. [42] studied HE of single crystalline type 316 austenitic steel under tensile testing. Crack propagation path had complex characteristic for twinning-dominated $\langle 111 \rangle$ crystals – quasi-cleavage fracture occurred along different active $\{111\}$ planes and zigzag fracture surface was observed [42]. They also checked out that HE was assisted by the localization of diffusible hydrogen to twin boundaries. Similar zigzag crack path is observed in 100h-H-charged and tested UFG-CrNiTi specimens (in hydrogen-assisted surface layer) (Figs. 14c and 14d). But change in crack path direction happens not in places of intersection of twin systems (as in case of $\langle 111 \rangle$ single crystal [42]), but on grain or subgrain boundaries.

Transgranular cleavage fracture elements associated with cracking along twin boundaries are also observed in tensile-tested UFG-CrNiTi steel specimens after hydrogen-charging for 5, 10, and 20 hours (Fig. 14b). But lower hydrogen concentration and, consequently, lower activity of twinning make this process less frequent compared to longer hydrogen saturation regimes. A large portion of intergranular fracture in specimens charged for 20 h or less testify to inhomogeneous hydrogen distribution along UFG structure. Isolated dislocations, dislocation tangles, vacancy complexes, low- and high-angle boundaries all act as trapping-sites for hydrogen atoms. The existence of intergranular cracks evidences predominant hydrogen accumulation by boundaries. After 5 h of H-charging, the average size of grains with intergranular fracture $d = 1.22 \mu\text{m}$, measured using SEM images, is a two-times larger than the mean size of subgrains (520 nm) revealed by TEM (Table 2). This allowed us to assume that at low saturation duration (less than 20 hours), hydrogen distribution in UFG structure is very inhomogeneous and diffusion occurs predominantly along the high-angle boundaries. At longer H-charging (40-100 hours), a high density of intragranular defects, induced by severe plastic deformation during ABC-pressing, contributes to trapping and fast accumulation of hydrogen atoms in subgrain interiors. From this point of view, refinement of the structure and producing of high density of trapping sites for hydrogen atoms in grain bodies reduce the difference in intergranular and transgranular hydrogen diffusion in UFG materials. Hereby, the UFG structure provides low difference in hydrogen distribution between

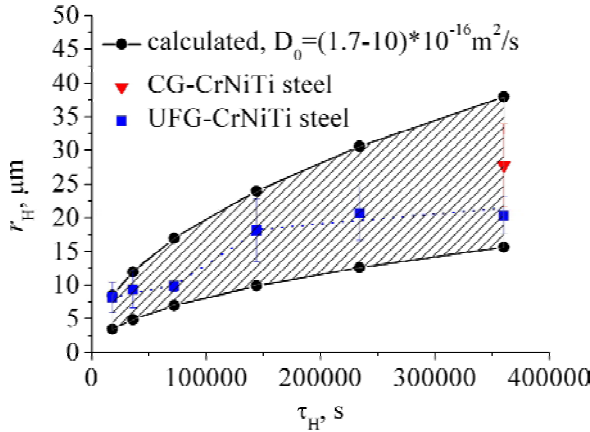


Fig. 16. Comparison of the values r_H , width of hydrogen-affected surface layer, estimated using $2\sqrt{D_0\tau_H}$ -criterion and from the observation of fracture surfaces of CG-CrNiTi and UFG-CrNiTi specimens.

boundaries and grain bodies, which is inherent in coarse grained materials [49].

Assuming hydrogen atoms occupy octahedral sites, the distance of hydrogen diffusion in fcc lattice of the steels (hydrogen-affected depth r_H) can be expressed by $r_H = 2\sqrt{D_0\tau_H}$, where diffusivity $D_0 = (1.7-10.0) \times 10^{-16} \text{ m}^2/\text{s}$ [6,33,50,51]. The comparison of the estimated values r_H and experimentally found width of hydrogen-affected regions from the observation of fracture surfaces of UFG-CrNiTi steel specimens is given in Fig. 16. Important conclusions follow from the analysis of Fig. 16:

(i) The plastic deformation in UFG-CrNiTi steel is not high, so tensile deformation to fracture lasts about 30 minutes. During straining, a stress-assisted diffusion of hydrogen atoms occurs in depth of the specimen. For this reason, experimentally found values r_H are slightly overestimated and can be assumed as $r_H = r_{H0} + r_H(\epsilon)$, where r_{H0} and $r_H(\epsilon)$ —distances of hydrogen diffusion during charging and during following tensile testing, respectively. We believe the value $r_H(\epsilon)$ is not high compared to r_{H0} because hydrogen-charging duration lasts much longer than following straining. We also take into account that the total tensile elongation for UFG steel is not influenced by hydrogen-charging, so the values r_{H0} are almost equal for every H-charging duration. Therefore, we assume this effect insignificant for further discussion in this section.

(ii) For hydrogen-charging up to 40 hours, estimated and experimentally found values r_H changes in similar way. But for longer H-saturation, the increment $\Delta r_H / \Delta t_H$ in UFG-CrNiTi specimens is much lower than that predicted by $2\sqrt{D_0\tau_H}$ -criterion. Strictly speak-

ing, the hydrogen-assisted layer does not grow with charging duration higher than 40 hours (Fig. 16). This is accordant with microstructural evolution of the UFG structure described in previous sections, namely, with coarsen, redistribution of dislocations and decrease in fraction of low-angle misorientations in UFG structure. With increase in hydrogen-charge duration (hydrogen concentration in surface layers), new hydrogen-driven dislocation configurations, subboundaries and boundaries create new trapping sites for hydrogen atoms directly during saturation process and, therefore, suppress further growth of hydrogen-assisted layers.

(iii) Hydrogen-affected depth r_H is higher for coarse-grained than that for UFG-CrNiTi steel being H-charged and tensile tested in similar regimes (data for 100 h-charging is available only). First, this discrepancy could be associated with difference in density of trapping sites for hydrogen atoms in CG and UFG structures (boundaries and defects of crystal lattice). Therefore, producing of UFG structures realizes higher “effective solubility” and lower “effective diffusivity” of hydrogen compared to traditional values for austenite. Second, different sizes of depth r_H could follow from the difference in tensile deformation duration for CG and UFG specimens (about 30 min for UFG specimens and 3.5 hours for CG one). Stress-induced diffusion of hydrogen atoms during tension could also increase hydrogen-affected depth in CG-specimen.

4. CONCLUDING REMARKS

We experimentally observed the effect of electrolytic hydrogen-charging (in NaCl water-solution for 100 hours) on tensile properties, deformation mechanisms and fracture of two austenitic CrNiMo and CrNiTi stainless steels processed by high-temperature ABC-pressing.

As a result of high-temperature plastic deformation, the ultrafine-grained austenitic structures with the average element size of 200 nm for CrNiMo and 520 nm for CrNiTi steel were produced. The refinement of the structure provides high strength properties in the steels ($\sigma_{0.2} = 1000 \text{ MPa}$ for UFG-CrNiMo steel and $\sigma_{0.2} = 790 \text{ MPa}$ for UFG-CrNiTi steel), but strongly reduces their elongation to fracture ($\delta = 5\%$ for UFG-CrNiMo steel and $\delta = 10\%$ for UFG-CrNiTi steel) as compare to coarse-grained analogous.

Hydrogen-charging up to 100 hours weakly influences stages of plastic flow, strength properties and elongation of the steels with UFG structures. These data evidence that strain-associated refinement of the structure, namely, the high density of

deformation defects and strain-induced low- and high-angle boundaries, does not provoke hydrogen embrittlement in CrNiTi and CrNiMo steels. Despite this fact, surface saturation of the steel specimens with hydrogen strongly influences microstructure, tensile deformation mechanisms and fracture micromechanisms in UFG-steels.

Hydrogen-charging provokes partial relaxation of highly defective UFG structure produced by ABC-pressing. Hydrogen-charging changes the relation between low- and high-angle misorientations in ultrafine-grained structure of both steels and decreases fraction of low-angle continual misorientations in steel structures. TEM analysis demonstrates partial annihilation and rearrangement of dislocations into dislocation tangles as a result of hydrogen-charging. Such hydrogen-induced relaxation and coarsening processes occur in ultrafine-grained structure of UFG-CrNiMo and UFG-CrNiTi steels without any external stresses applied to the specimens and are associated with hydrogen effect on nonequilibrium defect subsystem formed the steels during ABC-pressing.

Hydrogen-charging promotes to mechanical twinning and deformation-induced $\gamma \rightarrow \varepsilon$ martensitic transformation in the UFG steels. These two mechanisms are strongly dependent on stacking-fault energy of the ultrafine-grained steel. UFG-CrNiTi steels with lower SFE is more familiar with deformation twinning and deformation-induced $\gamma \rightarrow \varepsilon$ martensitic transformation than UFG-CrNiMo one.

The micromechanisms of the fracture in hydrogen-assisted layers of the steels are compositional and grain-size dependent values. In stable against deformation-induced transformation CrNiMo steel, the refinement of grain structure suppresses surface hydrogen-assisted cracking of the specimens. No visible brittle layers were detected in hydrogen-charged CG-CrNiMo and UFG-CrNiMo specimens. For metastable CrNiTi steel, hydrogen-charging is accompanied with the formation of brittle surface layers on side surfaces of the specimens. For UFG-CrNiTi specimens, the tensile fracture mode in such surface layers changes depending on hydrogenation duration: from mixed intergranular and transgranular cleavage mechanism in specimens tensile tested after 20 h-charging to transgranular cleavage one after longer H-saturation. Unlike extended regions of quasi-cleavage fracture in CG-CrNiTi specimens, plane facets (cleavages) in hydrogen-assisted layers of UFG specimens has submicron size, which is one-order of value with subgrain sized in UFG-CrNiTi steel.

ACKNOWLEDGEMENTS

The part of the research, which concerns hydrogen effect on properties of coarse-grained CrNiMo-steel, was performed within the frame of the Fundamental Research Program of the State Academies of Sciences for 2013-2020, line of research III.23. The research of the ultrafine-grained steels was supported by the Russian Foundation for Basic Researches (project No. 16-08-00926). The studies were conducted using the equipment of the Institute of Strength Physics and Materials Science (NANOTECH center). The authors thanks Dr. I.V. Ratochka and Dr. I.P. Mishin for providing ABC-pressing of the steel.

REFERENCES

- [1] M. Nagumo, *Fundamentals of hydrogen embrittlement* (Springer, Singapore, 2016).
- [2] K.H. Lo, C.H. Shek and J.K.L. Lai // *Mater. Sci. Eng. R* **65** (2009) 39.
- [3] C. San Marchi, In: *Gaseous hydrogen embrittlement of materials in energy technologies, V. 1. The problems, its characterization and effects on particular alloy classes*, ed. R.P. Gangloff and B.P. Somerday (Woodhead Publishing, 2012) p. 592.
- [4] L. Zhang, Z. Li, J. Zheng, Y. Zhao, P. Xu, C. Zhou and X. Li. // *Int. J. Hydr. Energy* **38** (2013) 8208.
- [5] D. Eliezer, D.G. Chakrapani, C.J. Altstetter and E.N. Pugh // *Met. Trans. A* **10** (1979) 935.
- [6] Y. Wang, X. Wang, J. Gong, L. Shen and W. Dong // *Int. J. Hydr. Energy* **39** (2014) 13909.
- [7] T. Michler, C.S. Marchi, J. Naumann, S. Weber and M. Martin // *Int. J. Hydr. Energy* **37** (2012) 16231.
- [8] T. Michler, J. Naumann, M. Hock, K. Berreth, M.P. Balogh and E. Sattler // *Mater. Sci. Eng. A* **628** (2015) 252.
- [9] H.K. Birnbaum and P. Sofronis // *Mater. Sci. Eng. A* **176** (1994) 191.
- [10] S. Lynch // *Corros. Rev.* **30** (2012) 105.
- [11] D.K. Han, A.I. Hwang, W.J. Byeon, S.J. Noh and D.-W. Suh // *Metallurg. Mater. Trans. A* **48** (2017) 5211.
- [12] Y. Mine, K. Tachibana and Z. Horita // *Mater. Sci. Eng. A* **528** (2011) 8100.
- [13] E. Astafurova, G. Maier, E. Melnikov, V. Koshovkina, V. Moskvina, A. Smirnov and V. Bataev // *AIP Conf. Proc.* **1683** (2015) 020014.

- [14] A. Macadre, K. Tsuboi, N. Nakada, T. Tsuchiyama and S. Takaki // *Proc. Mater. Sci.* **3** (2014) 350.
- [15] A. Macadre, N. Nakada, T. Tsuchiyama and S. Takaki // *Int. J. Hydr. Energy* **40** (2015) 10697.
- [16] Y. Mine, N. Horita, Z. Horita and K. Takashima // *Int. J. Hydr. Energy* **42** (2017) 15415.
- [17] Y. Mine, K. Tachibana and Z. Horita // *Metallurg. Mater. Trans. A.* **41** (2010) 3110.
- [18] S. Chen, M. Zhao and L. Rong // *Mater. Sci. Eng. A.* **594** (2014) 98.
- [19] S.-L. Chou and W.-T. Tsai // *Mater. Sci. Eng. A.* **270** (1999) 219.
- [20] K. Takasawa, R. Ikeda, N. Ishikawa and R. Ishigaki // *Int. J. Hydr. Energy* **37** (2012) 2669.
- [21] A. Belyakov, T. Sakai, H. Miura and R. Kaibyshev // *ISIJ Int.* **39** (1999) 592.
- [22] J. Yamabe, O. Takakuwa, H. Matsunaga, H. Itoga and S. Matsuoka // *Int. J. Hydr. Energy* **42** (2017) 13289.
- [23] E.V. Melnikov, E.G. Astafurova, G.G. Maier and V.A. Moskvina // *AIP Conf. Proc.* **1909** (2017) 020135.
- [24] S.K. Varma, J. Kalyanam, L.E. Murr and V. Srinivas // *J. Mater. Sci. Let.* **13** (1994) 107.
- [25] E.G. Astafurova, E.V. Melnikov, S.V. Astafurov, I.V. Ratochka, I.P. Mishin, G.G. Maier, V.A. Moskvina, G.N. Zakharov, A.I. Smirnov and V.A. Bataev // *Phys. Mesomech.* **21(2)** (2018) 103, In Russian.
- [26] D.B. Williams and C.B. Carter, *Transmission Electron Microscopy. Textbook for Materials Science* (Springer, New-York, 2009).
- [27] A. Belyakov, T. Sakai and H. Miura // *ISIJ Int.* **40(Supplement)** (2000) S164.
- [28] K. Tomimura, S. Takaki, S. Tanimoto and Y. Tokunaga // *ISIJ Int.* **31** (1991) 721.
- [29] *Martensite: a tribute of Morris Cohen*, ed. by G.B. Olson and W.S. Owen (ASTM international, PA, USA, 1992).
- [30] M.A. Meyers, A. Mishra and D.J. Benson // *Prog. Mater. Sci.* **51** (2006) 427.
- [31] D.G. Morris, M.A. Munos-Morris and I. Gutierrez-Urrutia // *Mater. Sci. For.* **633-634** (2010) 263.
- [32] A.A. Nazarov, A.E. Romanov and R.Z. Valiev // *Nanostr. Mater.* **4** (1994) 93.
- [33] I.M. Robertson, H.K. Birnbaum and P. Sofronis, In: *Dislocation in Solids*, ed. by J.P. Hirth and L. Kubin (Elsevier, New-York, 2009) p. 251.
- [34] I.M. Robertson // *Eng. Frac. Mech.* **68** (2001) 671.
- [35] E.G. Astafurova, V.A. Moskvina, G.G. Maier, E.V. Melnikov, G.N. Zakharov, S.V. Astafurov and H.J. Maier // *Scripta Mater.* **136** (2017) 101.
- [36] F.J. Humphreys and M. Hatherly, *Recrystallization and related annealing phenomena* (Elsevier, Oxford, 2004).
- [37] V.M. Shyvanyuk, Y. Mine and S.M. Teus // *Scripta Mater.* **67** (2012) 979.
- [38] J.W. Christian and S. Mahajan // *Prog. Mater. Sci.* **39** (1995) 1.
- [39] C.G. Rhodes and A.W. Thompson // *Met. Trans. A.* **8** (1977) 1901.
- [40] A.F. Padilha, R.L. Plaut, P.R. Rios // *ISIJ Int.* **43** (2003) 135.
- [41] H. Oettel and U. Martin // *Int. J. Mater. Res.* **97** (2006) 1642.
- [42] M. Koyama, E. Akiyama, T. Sawaguchi, K. Ogawa, I.V. Kireeva, Y.I. Chumlyakov and K. Tsuzaki // *Corrosion Sci.* **75** (2013) 345.
- [43] Y.H. Chang, C. Luo, C.A. Chen and S.X. Chen // *Mater. Sci. Eng. A.* **577** (2013) 23.
- [44] P.J. Ferreira, I.M. Robertson and H.K. Birnbaum // *Acta Mater.* **47** (1999) 2991.
- [45] V.G. Gavriluk, V.N. Shivanyuk and J. Foct // *Acta Mater.* **51** (2003) 1293.
- [46] Y.T. Zhu, X.Z. Liao and X.L. Wu // *Prog. Mater. Sci.* **57** (2012) 1.
- [47] S. Ganesh Sundara Raman and K.A. Padmanabhan // *J. Mater. Sci. Let.* **13** (1994) 389.
- [48] P. Hubner, R. Kiessling, H. Biermann and A. Vinogradov // *Int. J. Mater. Res.* **97** (2006) 11.
- [49] P. Rozenak, L. Zevin and D. Eliezer // *J. Mater. Sci.* **19** (1984) 567.
- [50] P. Rozenak and R. Bergman // *Mater. Sci. Eng. A.* **437** (2006) 366.
- [51] S. Sugiyama, H. Ohkubo, M. Takenaka, K. Ohsawa, M.I. Ansari, N. Tsukuda and E. Kuramoto // *J. Nucl. Mater.* **283-287** (2000) 863.